Mixing-demixing phase diagram for simple liquids in nonuniform electric fields

Jennifer Galanis[*] and Yoav Tsori[†]

Department of Chemical Engineering, Ben-Gurion University of the Negev, Beer-Sheva 84105, Israel

We deduce the mixing-demixing phase diagram for binary liquid mixtures in an electric field for various electrode geometries and arbitrary constitutive relation for the dielectric constant. By focusing on the behavior of the liquid-liquid interface, we produce simple analytic expressions for the dependence of the interface location on experimental parameters. We also show that the phase diagram contains regions where liquid separation cannot occur under *any* applied field. The analytic expression for the boundary "electrostatic binodal" line reveals that the regions' size and shape depend strongly on the dielectric relation between the liquids. Moreover, we predict the existence of an "electrostatic spinodal" line that identifies conditions where the liquids are in a metastable state. We finally construct the phase diagram for closed systems by mapping solutions onto those of an open system via an effective liquid composition. For closed systems at a fixed temperature and mixture composition, liquid separation occurs in a finite "window" of surface potential (or charge density). Higher potentials or charge densities counterintuitively destroy the interface, leading to liquid mixing. These results give valuable guides for experiments by providing easily testable predictions for how liquids behave in nonuniform electric fields.

I. INTRODUCTION

Phase transitions describe fundamental transformations in substances, where material properties, such as viscosity and refractive index, often dramatically change. These changes are mediated not only by intrinsic thermodynamic variables (temperature, pressure, etc.), but also by external forces (gravitational [1], magnetic [2], and electric [3] fields and shear flows [4,5]). Scientific interest in using electric fields to alter phase behavior spans over half a century and has resulted in theories and experiments devoted to the application of uniform fields in dielectric liquid mixtures [3,6–13]. Unfortunately, the liquid-field coupling in uniform electric fields is very weak since in such cases variations in the field strength occur as a result of variations in the permittivity of the liquid. As a consequence, theories predict that even minuscule changes to the phase diagram require enormous applied voltages [3,6,9].

In contrast, recent theoretical and experimental results reveal that nonuniform fields can effectuate large changes in phase diagrams [14–16]. The externally produced spatial variations in field strength occur even in homogeneous materials and lead to liquid rearrangement that can potentially induce liquid-liquid separation. High-gradient fields readily emerge from a modest potential or surface charge on misaligned plate capacitors as well as from small objects with high surface curvature, like nanowires and colloids [14–16]. Thus the relative ease of creating nonuniform fields underscores the potential to profoundly influence the behavior of complex liquids.

The challenge of nonuniform fields, however, resides in distinguishing true liquid-liquid phase separation from mere concentration gradients. In the more common case of uniform fields, the free energy has a double-well form with two coexisting minima. Since the system possesses translational invariance, the two liquids can replace each other in space without changing the total energy. This does not hold for nonuniform fields where translational invariance is broken. Here, the spatial location of the liquids is directly tied to the free energy, and as a consequence, the total free energy can have a single minimum even with two-phase coexistence. We point out that not all spatially nonuniform fields display this property, as, for example, in the case of random-field [17] and periodic-field [18] Ising models.

To overcome the difficulty of determining a transition, we defined phase separation by observing a *local* property—the behavior of the interface. Using this perspective, we derived analytic expressions for predicting the location of the interface from experimental parameters. We additionally adapted the standard methods used in creating phase diagrams and found the electrostatic equivalent of binodal and spinodal lines as well as critical points. The methods presented here can, in principle, apply to any geometry, and we explicitly give results for three basic electrode shapes: wedge, cylinder, and sphere. Furthermore, these methods can incorporate an arbitrarily complicated dielectric relation for the liquid composition, provided that derivatives to the expression exist.

The article is arranged as follows. We describe the theory for liquid mixtures with electric fields in Sec. II and briefly review general properties of phase diagrams in the absence of external fields in Sec. III. In Sec. IV, we introduce a useful definition of phase separation in an electric field that is essential for simplifying theoretical expressions. In Sec. V, we assume that phase separation exists and derive simple expressions for the location of the liquid-liquid interface. The mixing-demixing regions of the phase diagram as well as the dividing "electrostatic binodal" line are discussed in Sec. VI, while the theoretical stable-metastable states and dividing "electrostatic spinodal" line are presented in Sec. VII. Finally, we discuss important differences between open and closed systems in Sec. VIII.

II. THEORY

Using a mean-field approach, we consider a binary mixture of two liquids, *A* and *B*, in an electric field **E**, and write the

---

[*]galanis@bgu.ac.il
[†]tsori@bgu.ac.il

total free energy $\mathcal{F}$ for a volume V as

$$\mathcal{F} = \int_V (\mathcal{F}_m + \mathcal{F}_e)\, dV, \qquad (1)$$

where $\mathcal{F}_m$, and $\mathcal{F}_e$ are the free energy densities for mixing and electrostatics, respectively.

The liquids, in the absence of an electric field, can mix or demix due to a competition between entropy and enthalpy, where the temperature T adjusts the relative balance. For concreteness, we use the following Landau free energy of mixing $\mathcal{F}_m = kT f_m/Nv$, where the expansion is performed around the critical volume fraction ϕ_c,

$$f_m \approx (2 - N\chi)(\phi - \phi_c)^2 + \tfrac{4}{3}(\phi - \phi_c)^4 + \text{const}, \qquad (2)$$

where k is Boltzmann's constant, ϕ, such that $0 < \phi < 1$, is the volume fraction of component A, and $\chi \sim 1/T$ is the Flory interaction parameter [19]. Without loss of generality, we set $\phi_c = 0.5$ and $N\chi = 2T_c/T$, where T_c is the critical temperature. Simple liquids have $N = 1$, while polymers are composed of $N > 1$ monomers with volume v. Here, we consider the symmetric simple liquid $N = N_A = N_B = 1$. Real interfaces consist of a gradual change in composition. In contrast, f_m generates an interface marked by a discontinuity in composition. We find, however, that the discontinuity greatly simplifies the analysis that follows.

For electrostatics, the free energy $\mathcal{F}_e = kT f_e/Nv$ is given by

$$\mathcal{F}_e = \pm \tfrac{1}{2}\varepsilon_0 \varepsilon(\phi)|\nabla\psi|^2, \qquad (3)$$

where ε_0 is the vacuum permittivity and ψ is the electrostatic potential ($\mathbf{E} = -\nabla\psi$). The positive (negative) sign corresponds to constant charge (potential) boundary conditions.

The dielectric permittivity at zero frequency $\varepsilon(\phi)$ depends on the relative liquid-liquid composition. For clarity in the discussion, we mainly consider a linear relation, $\varepsilon(\phi) = (\varepsilon_A - \varepsilon_B)\phi + \varepsilon_B$, where ε_A and ε_B are the dielectric constants for pure liquids A and B, respectively. Excluding the possibility of critical behavior in $\varepsilon(\phi)$ in the immediate vicinity of the liquid's critical point (ϕ_c, T_c) [20,21], the measured $\varepsilon(\phi)$ often approximates a quadratic function for various liquid combinations [9,10]. We, therefore, highlight some significant changes in the results that occur with higher order $\varepsilon(\phi)$ relations.

To determine the equilibrium state in the presence of a field, we minimize $\mathcal{F}$ with respect to ϕ and ψ using calculus of variations and obtain the Euler-Lagrange equations

$$\frac{\delta\mathcal{F}}{\delta\psi} = \nabla \cdot [\varepsilon_0 \varepsilon(\phi)\nabla\psi] = 0, \qquad (4)$$

$$\frac{\delta\mathcal{F}}{\delta\phi} = \mathcal{F}_m' - \frac{\varepsilon_0}{2}\varepsilon'(\phi)|\nabla\psi|^2 - \tilde{\mu} = 0, \qquad (5)$$

where the prime ($'$) represents the derivative with respect to ϕ. The first equation is Laplace's equation for the potential ψ, while the second equation gives the composition distribution ϕ. Both $\varepsilon(\phi)$ and ψ couple the two equations.

The Lagrange multiplier $\tilde{\mu} = kT\mu/Nv$ in Eq. (5) differentiates between open and closed systems. For a closed system (canonical ensemble), μ is adjusted to satisfy the mass conservation constraint, $\langle\phi\rangle = \phi_0$, where ϕ_0 is the average composition. When the system under consideration is coupled
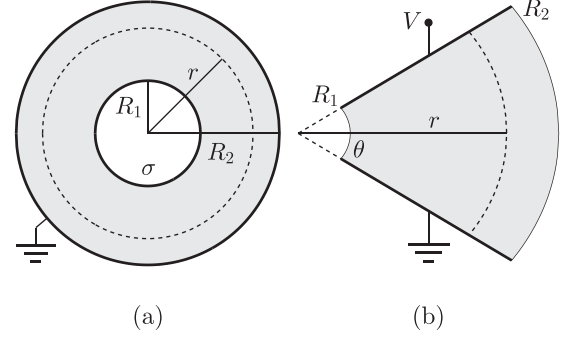

FIG. 1. Model systems. (a) Cross section through the diameter of concentric cylinders or spheres with surface charge density σ. The distance r is measured from the center of the cylinder/sphere, and the boundaries are located at R_1 and R_2. (b) Cross section of two flat-plate electrodes with an opening angle θ and potential difference V. Distance r is measured from the "intersection" of the two plates, and the boundaries R_1 and R_2 mark the ends of the plates. Shading shows the space occupied by the liquid mixture.

to an infinite reservoir at composition ϕ_0, $\mu = \mu_0(\phi_0)$ is the chemical potential of the reservoir.

We conduct detailed investigations of the phase transition with three simple yet fundamental shapes—cylinder, sphere, and wedge. A closed system with cylindrical geometry consists of two concentric cylinders with radii R_1 and R_2, where $R_2 \to \infty$ produces an open system [Fig. 1(a)]. We impose cylindrical symmetry such that $\phi = \phi(r)$ and $\psi = \psi(r)$, where r is the distance from the inner cylinder's center. Furthermore, the prescribed charge density σ on the inner cylinder allows integration of Gauss's law to obtain an explicit expression for the electric field. By using a similar construction for spherical geometry we find that the electric field for both cylindrical and spherical configurations is $\mathbf{E}(r) = \sigma R_1^n/(\varepsilon_0 \varepsilon(\phi)r^n)\hat{\mathbf{r}}$, where $n = 1$ and 2 for cylinders and spheres, respectively. Combining this result with $\mathbf{E} = -\nabla\psi$ in Eq. (5), we obtain a single equation determining the composition profile $\phi(r)$:

$$f_m' - \frac{Nv}{2kT\varepsilon_0}\left(\frac{\sigma R_1^n}{r^n}\right)^2 \frac{\varepsilon'(\phi)}{\varepsilon(\phi)^2} - \mu = 0. \qquad (6)$$

The wedge geometry consists of two "misaligned" flat plates with an opening angle θ [Fig. 1(b)]. Using a constant potential boundary condition, we obtain an electric field $\mathbf{E}(r) = (V/r\theta)\hat{\vartheta}$, where V is the potential difference across the electrodes, r is the distance from the imaginary intersection of the two plates, and ϑ is the azimuthal angle. Combining this result with Eq. (5), we obtain

$$f_m' - \frac{Nv}{2kT}\left(\frac{V}{r\theta}\right)^2 \varepsilon_0 \varepsilon'(\phi) - \mu = 0. \qquad (7)$$

In this article we mainly present results for cylindrical geometry. This geometry intrinsically presents a mathematically unsavory dependence of f_e on ϕ [via $\varepsilon(\phi)$] and, therefore, creates more complicated solutions than, for example, in the wedge. Also, the difference in equational form between the cylinder and the sphere does not present new information for

discussion. The methods presented here can easily be adapted to both wedge and sphere geometries.

As will become evident, the precise surface charge density (surface potential) necessary to induce a transition depends on experimental parameters like the size and relative concentration of the liquid molecules, size of the charged material, temperature, etc. We consider a wide range of surface charges σ, from approximately 0 up to 2×10^{-3} C/m^2 (equivalent to $1.25 \times 10^{-2} e$/nm^2). For comparison, colloidal particles immersed in the nonpolar phase of an inverse-micelle liquid have been measured to have high surface potentials, with an estimate of $200e$ to $900e$ charges [22]. This amount of charge on a colloid could induce phase separation in a binary mixture if its composition is close enough to the demixing curve. The demixed liquid layer surrounding the colloid is predicted to be several tens to hundreds of nanometers thick, thereby altering the local environment of the colloid in an otherwise mixed liquid suspension. Of course, having the ability to externally apply a field, for example, via an electrode, can be useful in some applications.

III. PHASE DIAGRAM WITHOUT AN ELECTRIC FIELD

We briefly discuss some features of the mixing-demixing phase diagram in the absence of electric fields that are essential in the derivations below. A "double-well" function [for example Eq. (2) when $T < T_c$] possesses two local minima, one local maximum, and two inflection points located between the maximum and each minimum.

To ascertain the minimum of f_m at constant T, we find the solution to $f'_m = 0$ [Fig. 2(c)] that also satisfies $f_m^{(2)} > 0$ [Fig. 2(d)], where the derivatives are taken with respect to ϕ_0. The two solutions $\phi_b(T) = 1/2 \pm \sqrt{3(T_c - T)/4T}$ for each $T < T_c$ create the binodal curve [thick solid line in Fig. 2(a)]. Fluids demix if the initial conditions (ϕ_0, T) are under the binodal curve and mix if they are above this curve. There in fact exists a third solution to $f'_m = 0$ [Fig. 2(c)]—the local maximum at concentration $\phi_u(T)$ [dashed line in Fig. 2(a)]. Even though this solution is physically unstable [$f_m^{(2)}(\phi_u) < 0$; Fig. 2(d)], it will be useful in subsequent sections. If the local minima satisfy $f_m^{(2)} > 0$ and the local maximum satisfies $f_m^{(2)} < 0$, then there must exist inflection points between the extrema that satisfy $f_m^{(2)} = 0$ [Fig. 2(d)]. These solutions $\phi_s(T) = 1/2 \pm \sqrt{(T_c - T)/4T}$ for each $T < T_c$ create the spinodal line [dash-dotted line in Fig. 2(a)] and describe liquid behavior dynamically. If the initial point (ϕ_0, T) is located below the spinodal curve, then the liquids demix spontaneously. If, however, ϕ_0 exists between ϕ_b and ϕ_s, then the liquid can be "stuck" in a local minimum, resulting in a metastable mixed state.

At the critical point (ϕ_c, T_c) the shape of f_m changes from having a single minimum to double minima. As T increases to T_c, the two minima ϕ_b, the two inflection points ϕ_s, and the maximum ϕ_u converge and convert into a single minimum ϕ_c. To meet these requirements the critical point must satisfy $f'_m = f_m^{(2)} = f_m^{(3)} = 0$ and $f_m^{(4)} > 0$. Figures 2(c) and 2(d) display two of the four requirements. Finally, the light solid line in Fig. 2(a) shows the single solution $\phi_i(T)$ to $f'_m = 0$ above the critical point.
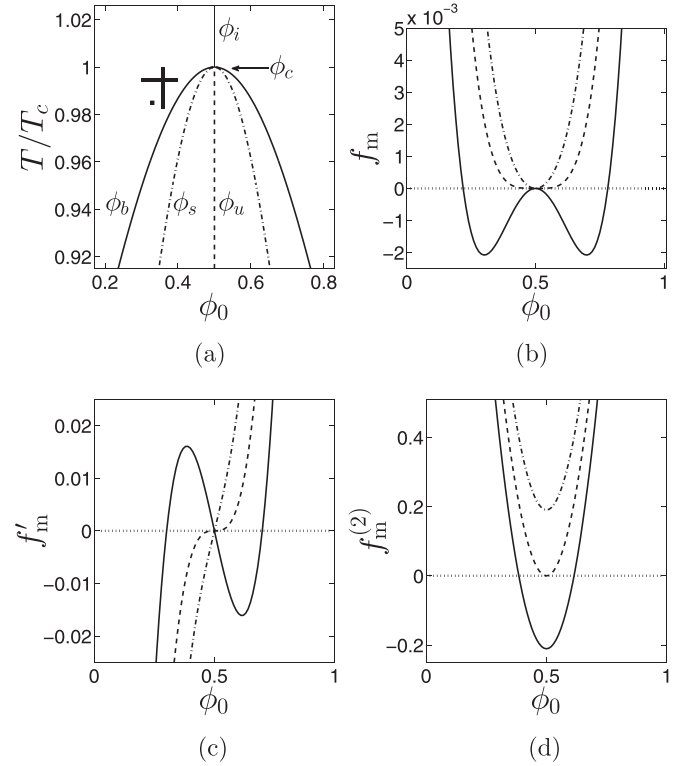

FIG. 2. Free energy of mixing f_m. (a) Phase diagram in the ϕ_0-T plane showing the zero-field binodal curve (ϕ_b; thick solid line), spinodal curve (ϕ_s; dash-dotted line), unstable solution (ϕ_u; dashed line), critical point ϕ_c, and minimum of f_m above T_c (ϕ_i; thin solid line). Symbols mark the location of data in Fig. 4(a), while horizontal and vertical bars mark the location of data in Figs. 4(c) and 4(d), respectively. (b)–(d) Plots of f_m and its derivatives with respect to ϕ versus ϕ_0 for T less than (solid line), equal to (dashed line), and greater than (dash-dotted line) T_c. In this and in all other figures $T_c = 298$ K, $\varepsilon_A = 5$, $\varepsilon_B = 3$, $R_1 = 1$ μm and $Nv = 1 \times 10^{-26}$ m^3.

IV. DEFINING PHASE SEPARATION

Nonuniform electric fields impose a nonuniform "pull" on the liquid mixture, manifesting as an r-dependent total free energy density $f(\phi, r) = f_m(\phi) + f_e(\phi, r) - \phi\mu$. The behavior of f can be conceptualized as a competition between mixing and electrostatic energies. As $r \to \infty$, the electric field is weak, $f_e \to 0$, and $f \approx f_m - \phi\mu$ governs liquid behavior. The solid line in Fig. 3(a) shows a typical example of $f(\phi, r)$ at a large value of r using $\phi_0 = 0.33$, $T/T_c = 0.98$, and $\sigma = 1.428 \times 10^{-3}$ C/m^2 in an open cylinder system. The minimum of $f(\phi, r)$, marked by a symbol, gives the value of $\phi(r)$ as $r \to \infty$, which in this case is 0.33. At the other distance extreme, $r = R_1$, the electric field is the strongest, and the dashed line in Fig. 3(a) shows the resulting $f(\phi, r)$. Note the dramatic difference in the value of $\phi(r)$ when the value of r is small (R_1) versus large.

By finding the minimum of f for all values of r, it is possible to construct the full concentration profile $\phi(r)$, where the solid line in Fig. 3(b) corresponds to the data from Fig. 3(a). Whether or not a phase transition occurs in the equilibrium solution resides in how the minimized $f(\phi, r)$ changes as r varies between the two distance extremes. Specifically, if there exists an $r = r_i$ where $R_1 \leqslant r_i \leqslant R_2$ and $f(\phi, r_i)$ contains
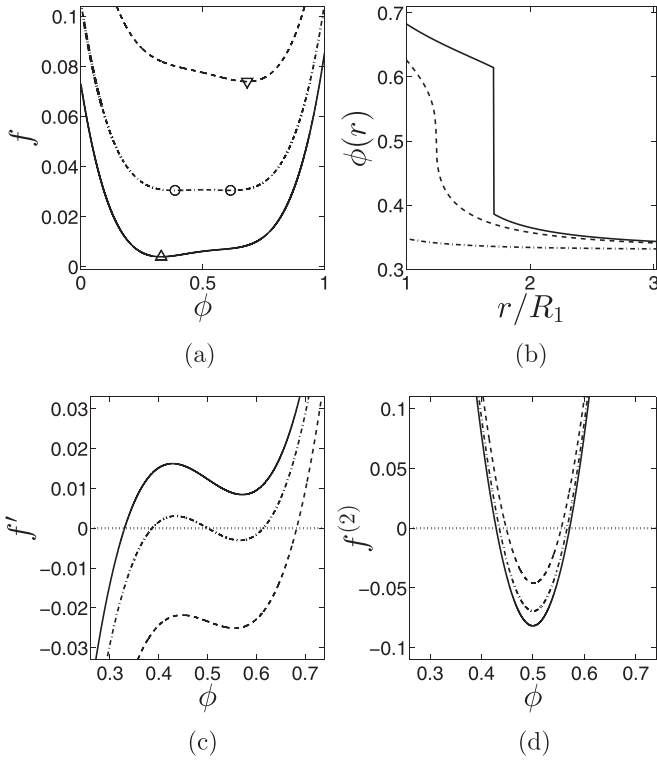
FIG. 3. Free energy density $f(\phi,r)$ for an open cylinder system, where (a), (c), and (d) show f, f', and $f^{(2)}$, respectively, versus ϕ at distance $r = R_1$ (dashed line), r_i (dash-dotted line), and a large value (solid line) for $\phi_0 = 0.33$, $T/T_c = 0.98$, and $\sigma = 1.428 \times 10^{-3}$ C/m². Symbols in (a) show the minima for each curve. (b) $\phi(r)$ versus normalized distance r. The solid line shows data from (a). The dash-dotted line has the same ϕ_0 and T as in (a) but with the smaller $\sigma = 0.540 \times 10^{-3}$ C/m². The dashed line has the same ϕ_0 and σ as in (a) but with the larger $T/T_c = 0.995$.
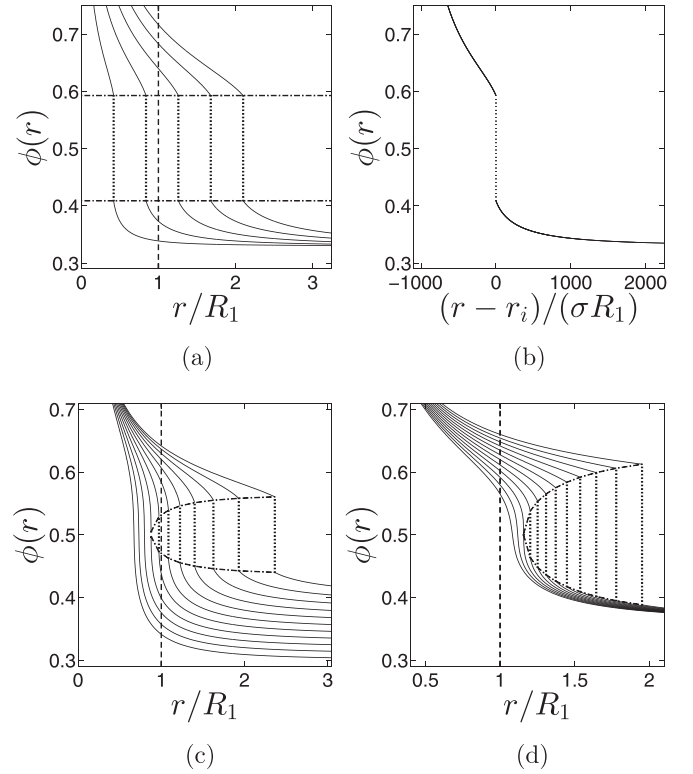

FIG. 4. Variation of concentration profiles $\phi(r)$ for an open cylinder system. (a) $\phi(r)$ versus normalized distance r for constant $\phi_0 = 0.33$, $T/T_c = 0.985$, and varying $\sigma = 0.4 \times 10^{-3}$ to 2.0×10^{-3} C/m² in 0.4×10^{-3} increments (lines, left to right). (b) Data in (a) collapse when plotted versus a rescaled distance $(r - r_i)/(\sigma R_1)$. (c) $\phi(r)$ versus r for constant $T/T_c \approx 0.994$, $\sigma = 1 \times 10^{-3}$ C/m², and varying $\phi = 0.3$ to 0.4 in 0.01 increments (lines, left to right). (d) $\phi(r)$ versus r for constant $\phi = 0.36$, $\sigma = 1 \times 10^{-3}$ C/m², and varying $T/T_c \approx 0.982$ to 1 in 0.0016 increments (lines, right to left).

two minima [see dash-dotted line in Fig. 3(a)], then r_i is an interface between the two liquids. Figure 3(b) illustrates how the two minima in $f(\phi,r_i)$ translate into a discontinuity at $\phi(r_i)$, thereby creating a distinct boundary between the two phases.

A closer inspection of $f(\phi,r)$ at $r = r_i$ reveals important mathematical features similar to those in $f_m(\phi)$ discussed in the previous section. The similarity is not surprising, since $f_m(\phi)$ is a component of $f(\phi,r)$. The dash-dotted lines in Figs. 3(a), 3(c), and 3(d) show that $f(\phi,r_i)$ possesses two local minima that we call ϕ_{iH} and ϕ_{iL}, one local maximum ϕ_u, and two inflection points that we call ϕ_{sH} and ϕ_{sL}. In addition, $f(\phi,r_i)$ can have critical behavior. We demonstrate that all these features at r_i behave analogously to those in Fig. 2(a) and show how to use this information to construct the mixing-demixing phase diagram with an electric field.

V. COMPOSITION PROFILES $\phi(r)$ AND LOCATION OF THE INTERFACE

Not all applied fields induce liquid demixing, and based on our definition of a phase transition, there are two possible causes. First, r_i exists in "virtual" ($r_i < R_1$ or $r_i > R_2$) rather than "real" space [dash-dotted line in Fig. 3(b)]. Second, f

contains a single minimum for *all* r, including r_i [dashed line in Fig. 3(b)].

We begin with the first cause. For a constant ϕ_0 and T, Fig. 3(b) shows that certain values of σ induce a transition, whereas others do not. In fact, there exists a transition σ_t that marks the lowest σ necessary for liquid-liquid separation. Figure 4(a) also shows how increasing σ moves the interface r_i to larger r, using an open cylinder system as an example. Noting that mathematical solutions exist for all r (including those distances in nonphysical space), the vertical dashed line in Fig. 4(a) at $r = R_1$ marks the surface of the cylinder. To the right of this line is real (physical) space, while to the left is the virtual space inside the electrode [or not between the plates as defined in Fig. 1(b) for wedge geometries]. This observation inspires an alternative definition: the surface charge density σ_t is the σ that places r_i exactly at R_1. We stress that profiles $\phi(r)$ at constant ϕ_0 and T in open systems with varying values of σ all collapse to a single curve when plotted versus a scaled distance $(r - r_i)/(\sigma R_1)$ [Fig. 4(b)].

Varying ϕ_0 (holding T and σ constant) and T (holding ϕ_0 and σ constant) reveals the second cause for no phase separation, illustrated in Figs. 4(c) and 4(d), respectively. In these cases, both the interface location r_i and the size of the discontinuity change. Importantly, the discontinuity can even
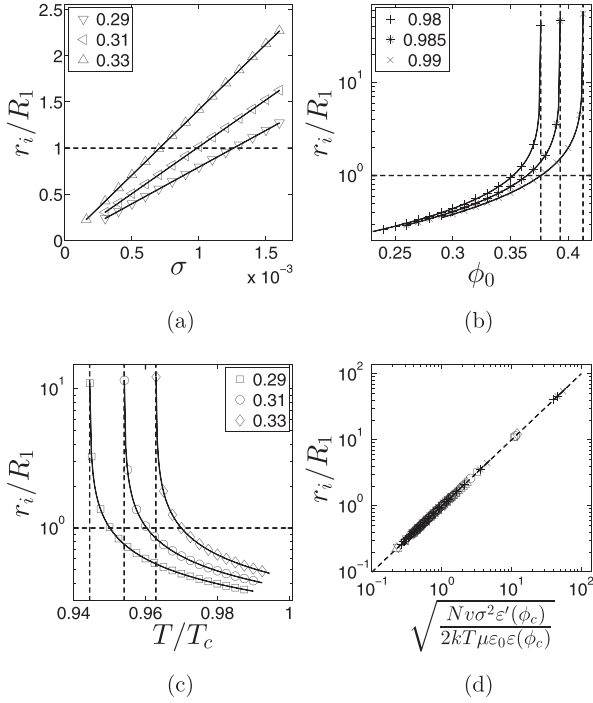
FIG. 5. Controlling the location of the interface r_i for an open cylinder system. (a) Normalized r_i versus σ [C/m^2] for various values of ϕ_0, where $T/T_c = 0.975$. (b) Normalized r_i versus ϕ_0 for various values of T/T_c, where $\sigma \approx 5.4 \times 10^{-4}$ C/m^2. (c) Normalized r_i versus T/T_c for various ϕ_0, where $\sigma \approx 5.4 \times 10^{-4}$ C/m^2. (d) Collapse of all data from (a)–(c) when r_i is plotted against Eq. (10). In (b) and (c), vertical dashed lines mark the binodal for the given values of ϕ_0 and T.

vanish as the high and low concentrations ϕ_{iH} and ϕ_{iL} at the interface merge to the same value at certain ϕ_0 or T. Note the remarkable similarity between the behavior of the discontinuity at r_i [dash-dotted lines in Figs. 4(c) and 4(d) and the binodal curve [Fig. 2(a)].

The location of the interface, once it exists, is controlled by ϕ_0, T, σ, and R_2. In general, r_i increases with increasing σ [Figs. 4(a) and 5(a)], increasing ϕ_0 [Figs. 4(c) and 5(b)], decreasing T [Figs. 4(d) and 5(c)], and increasing R_2 [discussed in Sec. VIII; Fig. 8(b)]. Besides solving the full $\phi(r)$ profile, a quicker method for determining the location of the interface r_i consists of solving the three equations [16,23]

$$f'_m(\phi_{iH}) - f'_e(\phi_{iH}, r_i) - \mu = 0,$$
$$f'_m(\phi_{iL}) - f'_e(\phi_{iL}, r_i) - \mu = 0,$$
$$f_m(\phi_{iH}) \pm f_e(\phi_{iH}, r_i) - \phi_{iH}\mu = f_m(\phi_{iL}) \pm f_e(\phi_{iL}, r_i) - \phi_{iL}\mu$$

$$(8)$$

for three unknowns: r_i and the high and low concentrations ϕ_{iH} and ϕ_{iL}, respectively, at r_i. The plus (minus) sign in the third equation is for constant charge (potential) boundary conditions. The first two equations find extremum points and are simply Eq. (6) or (7), depending on the system geometry. The third equation ensures that the free energy for the high concentration ϕ_{iH} is as favorable as the low concentration ϕ_{iL}.

An even simpler method for finding r_i consists of recalling that there exists a third solution to f': the local maxima

ϕ_u [Fig. 3(c)]. For cylindrical ($n = 1$) and spherical ($n = 2$) geometries, the explicit equation for $f' = 0$ is

$$0 = 4\left(1 - \frac{T_c}{T}\right)(\phi_u - \phi_c) + \frac{16}{3}(\phi_u - \phi_c)^3$$
$$- \frac{Nv}{2kT\varepsilon_0}\left(\frac{\sigma R_1^n}{r_i^n}\right)^2 \frac{\varepsilon'(\phi_u)}{\varepsilon(\phi_u)^2} - \mu. \tag{9}$$

If ϕ_u is known, then r_i can, in principle, be deduced from experimental parameters (ϕ_0, T, etc.). For now, we borrow ideas from the binodal curve and make the assumption $\phi_u = \phi_c = 0.5$, but we see later that ϕ_u indeed approximately equals ϕ_c under many conditions. Rearranging Eq. (9), we now have the useful relation

$$\left(\frac{\sigma R_1^n}{r_i^n}\right)^2 = -\mu \frac{2kT\varepsilon_0}{Nv}\frac{\varepsilon(\phi_c)^2}{\varepsilon'(\phi_c)}. \tag{10}$$

In open systems, this equation is further simplified by substituting $\mu = \mu_0(\phi_0) = f'_m(\phi_0, T)$. The lines in Figs. 5(a), 5(b), and 5(c) use Eq. (10) to solve r_i in an open cylinder system and reveal an excellent agreement with the solutions from Eqs. (8) (symbols). Figure 5(d) combines all data from Figs. 5(a), 5(b), and 5(c), revealing that the agreement spans many orders of magnitude.

The analogous equation for finding r_i in a wedge geometry is

$$\left(\frac{V}{\theta r_i}\right)^2 = -\frac{2kT\mu}{Nv\varepsilon_0\varepsilon'(\phi_c)}. \tag{11}$$

VI. STABILITY DIAGRAM AND ELECTROSTATIC BINODAL

If an electric field can cause phase separation in a region of ϕ_0-T space *above* the binodal curve, a natural question arises: What is the new stability diagram for a particular value of surface charge density σ? This can be constructed by holding σ constant and probing ϕ_0-T space for liquid-liquid demixing. Since the electric field breaks the symmetry of the free energy with respect to composition ($\phi_0 \to 1 - \phi_0$), the stability diagram is asymmetric with respect to $\phi_0 - \phi_c$. Figure 6(a) compares a typical stability curve for an open cylindrical system (solid line) to the binodal curve (dashed line). Clearly, nonuniform fields can produce large changes in the phase diagram.

Figure 6(b) shows the superposition of stability diagrams from a wide range of σ in an open cylindrical system, where the color indicates the transition σ_t for each point (ϕ_0, T). (Points beneath the binodal curve are omitted since phase separation occurs there without an electric field.) Figure 6(b) clearly illustrates two distinct regions in the ϕ_0-T plane. In the "demixed" region, there exists a σ_t for each (ϕ_0, T) such that any $\sigma \geqslant \sigma_t$ results in liquid demixing. In the "mixed" region, *no* σ exists that results in liquid demixing. Note how the mixed region extends well below T_c, indicating that simply setting $T < T_c$ is not sufficient to produce a phase transition with an electric field. We call the curve that divides these two regions the "electrostatic binodal."

To derive the electrostatic binodal, we draw inspiration from the "regular" binodal curve. The convergence of the
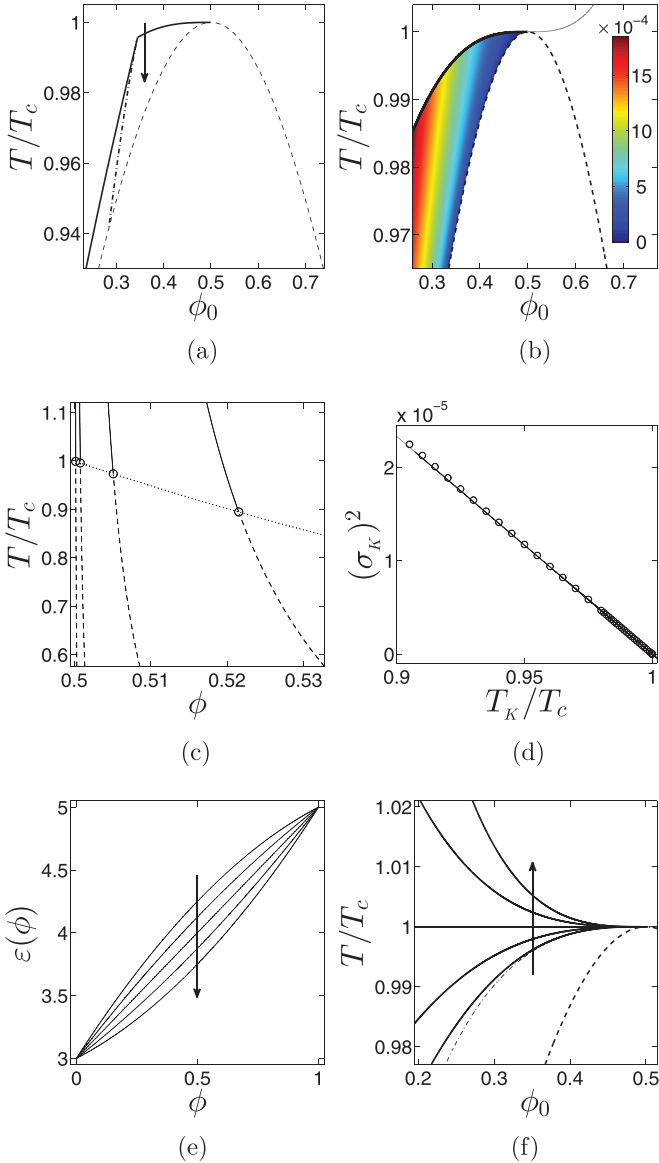
FIG. 6. (Color online) Electrostatic binodal in open systems. (a) Stability diagram (solid line) and electrostatic spinodal (dash-dotted line) in the ϕ_0-T plane for $\sigma = 1 \times 10^{-3}$ C/m². The dashed line is the binodal curve. The path of the arrow marks the location of data in Fig. 4(d). (b) Overlay of many stability diagrams, where color indicates transition σ_t (C/m²). The solid line is electrostatic binodal from Eq. (14), where thick and thin marks show where values of $\sigma_t = \sigma_K$ are real and imaginary, respectively. (c) Solutions ϕ_i (solid lines), ϕ_{iC} (symbols), and ϕ_u (dashed lines) to $f^{(3)} = 0$ versus T, where $\sigma = 0.5 \times 10^{-3}$, 1×10^{-3}, 2.5×10^{-3}, and 5×10^{-3} C/m² (lines, left to right). The dotted curve shows ϕ_{iC} for all σ. (d) Critical σ_K [C/m²] along the electrostatic binodal versus T_K. (e) Quadratic forms of $\varepsilon(\phi)$ versus ϕ, where the second derivative $\varepsilon^{(2)}(\phi) = -2$, -1, 0, 1, and 2 (arrow). (f) Solid lines show the electrostatic binodal for an open wedge system using the $\varepsilon^{(2)}(\phi)$ from (e) (arrow). The dash-dotted line shows the electrostatic binodal using Flory-Huggins theory for f_m and $\varepsilon^{(2)}(\phi) = -2$. The dashed line is the binodal curve.

interface concentrations ϕ_{iH} and ϕ_{iL} in Figs. 4(c) and 4(d) suggests the existence of a critical point at r_i. If there exists a critical point at r_i, then the two minima ϕ_{iH} and ϕ_{iL}, the

local maximum ϕ_u, and the two inflection points ϕ_{sH} and ϕ_{sL} converge to a single point ϕ_{iC}, resulting in $f'(r_i) = f^{(2)}(r_i) = f^{(3)}(r_i) = 0$ and $f^{(4)}(r_i) > 0$. We call the coordinates in the ϕ_0-T plane that produce a critical point at r_i the critical ϕ_K and critical T_K.

We now show one method for finding ϕ_K and T_K, using an open cylinder system as an example and beginning with $f^{(2)} = 0$:

$$2\left(1 - \frac{T_c}{T_K}\right) + 8(\phi_{iC} - \phi_c)^2 + \frac{Nv}{2kT_K\varepsilon_0}\frac{[\varepsilon'(\phi_{iC})]^2}{\varepsilon(\phi_{iC})^3}\left(\frac{\sigma R_1}{r_i}\right)^2 = 0. \quad (12)$$

The derivation of Eq. (10) depends on finding a ϕ that satisfies $f' = 0$ but does not specify ϕ as a local maximum or minimum. In particular, ϕ_{iC} also satisfies Eq. (10). We therefore substitute Eq. (10) for $(\sigma R_1/r_i)^2$ into Eq. (12), use $\mu = \mu_0(\phi_K) = f'_m(\phi_K, T_K)$ for an open system, and rearrange to obtain

$$\frac{T_K}{T_c} = \left[\frac{4(\phi_{iC} - \phi_c)^2 - \frac{8}{3}(\phi_K - \phi_c)^3 \frac{\varepsilon'(\phi_{iC})}{\varepsilon(\phi_{iC})}}{1 - 2(\phi_K - \phi_c)\frac{\varepsilon'(\phi_{iC})}{\varepsilon(\phi_{iC})}} + 1\right]^{-1}$$
$$\text{open cylinder.} \quad (13)$$

Note that as $\varepsilon' \to 0$, we recover the solution to $f_m^{(2)} = 0$, and $T_K \to T_c$ when ϕ_i equals the critical composition ϕ_c.

Proceeding, ϕ_{iC} must also satisfy $f^{(3)} = 0$ at r_i. Figure 6(c) shows the solutions to $f^{(3)} = 0$ for a wide range of T, where the curves from left to right are low to high σ. The values of ϕ_i (solid lines), ϕ_{iC} (symbols), and ϕ_u (dashed lines) form a continuous variation with T [Fig. 6(c)], analogous to ϕ_i, ϕ_c, and ϕ_u with f_m [Fig. 2(a)]. Since $\phi_{iC} \approx \phi_c$ [Fig. 6(c)], we can simplify Eq. (13) to obtain the expression for the electrostatic binodal in an open cylinder system:

$$\frac{T_K}{T_c} \approx \left[\frac{-\frac{8}{3}(\phi_K - \phi_c)^3 \frac{\varepsilon'(\phi_c)}{\varepsilon(\phi_c)}}{1 - 2(\phi_K - \phi_c)\frac{\varepsilon'(\phi_c)}{\varepsilon(\phi_c)}} + 1\right]^{-1} \text{ open cylinder.} \quad (14)$$

Interestingly, this equation depends only on ϕ_K and the functional form of $\varepsilon(\phi)$, and is independent of σ and r_i. This finding is a consequence of the self-similarity of solutions in open systems for a constant ϕ_0 and T, described in Sec. V and shown in Fig. 4(b). Moreover, the geometry difference between cylinders and spheres does not influence the electrostatic binodal. Equation (14) is, in fact, the same equation for the electrostatic binodal in an open sphere system, using the same assumptions.

The thick solid line in Fig. 6(b) shows the results from Eq. (14), as it accurately divides the ϕ_0-T plane into mixed and demixed regions. With each point (ϕ_K, T_K), there is an associated critical σ_K: the σ that places r_i exactly at R_1. It is important to recognize that σ_K is not constant along the electrostatic binodal: σ_K is 0 at $T_K = T_c$ and increases as T_K [Fig. 6(d)] and/or ϕ_K decreases. Figure 6(d) compares σ_K from calculations (symbols) versus σ_K derived from Eq. (10) using ϕ_K, T_K, and $r_i = R_1$ (line). Equation (14) predicts that the electrostatic binodal also exists for $\phi_0 > \phi_c$ [thin solid line in Fig. 6(b)]; however, the associated values of σ_K are imaginary and not possible in real physical systems.

The electrostatic binodal is a line of critical points, or simply a "critical line." This finding explains some curious observations found previously [16]: If ϕ_0 and/or T is changed such that the stability diagram for a constant σ is crossed on the boundary between the kink and (ϕ_c, T_c) [for example, the arrow in Fig. 6(a)], then r_i emerges at some distance *greater* than R_1 [Fig. 4(d)]. The kink marks $(\phi_K, T_K, \sigma = \sigma_K)$. The boundary of the stability diagram to the right of the kink is exactly the electrostatic binodal. On this boundary, σ is now *larger* than σ_K. In other words, σ is no longer the minimum surface charge that induces the transition; therefore, r_i necessarily emerges at some distance greater than R_1.

The open wedge system produces analogous results; however, we use the simplicity of the equations in this geometry to demonstrate the effects of quadratic $\varepsilon(\phi)$ relations [Fig. 6(e)]. Following the same reasoning as for an open cylinder system, we find the electrostatic binodal for an open wedge:

$$\frac{T_K}{T_c} = \left[\frac{\frac{4}{3}(\phi_K - \phi_c)^3 \frac{\varepsilon^{(2)}(\phi_c)}{\varepsilon'(\phi_c)}}{1 + (\phi_K - \phi_c)\frac{\varepsilon^{(2)}(\phi_c)}{\varepsilon'(\phi_c)}} + 1 \right]^{-1} \quad \text{open wedge.} \quad (15)$$

We add that ϕ_i, ϕ_{iC}, and ϕ_u exactly equal ϕ_c if $\varepsilon^{(2)}(\phi)$ and higher derivatives vanish. Note the similarity between Eq. (14) and (15), where the main difference is that higher derivatives of $\varepsilon(\phi)$ control the electrostatic binodal in the wedge geometry. Figure 6(f) shows how the electrostatic binodal for the wedge curves downwards to upwards as $\varepsilon^{(2)}(\phi_c)$ changes from negative to positive. And if $\varepsilon^{(2)}(\phi_c) = 0$, then T_K for the electrostatic binodal simply equals T_c for all ϕ_K. By comparing Fig. 6(e) to the results in Fig. 6(f), it is evident that small amounts of curvature in $\varepsilon(\phi)$ can create large changes in the electrostatic binodal, in agreement with previous findings [16].

We briefly discuss an alternate derivation presented in Ref. [16] to emphasize that we have not exhausted all possible relations between parameters. Beginning with $f^{(2)} = f^{(3)} = 0$ for $r_i = R_1$ and $\varepsilon^{(3)}(\phi) = 0$ in the wedge geometry, we obtain

$$\frac{T_K}{T_c} = 1 + \frac{N v \varepsilon_0 \varepsilon^{(2)}(\phi)}{8 k T_c} \left(\frac{V_K}{\theta R_1} \right)^2. \quad (16)$$

Interestingly, using the Flory-Huggins approximation for f_m results in exactly the same relation [Eq. (16)] as the Landau approximation. The differences between the two approximations instead arise when determining ϕ_K, where the biggest discrepancies occur, as expected, for values of ϕ_K that are far from ϕ_c [Fig. 6(f)].

VII. ELECTROSTATIC SPINODAL

We now turn the discussion to possible metastable states, recalling the meaning of the spinodal curve in the mean-field theory [24]. Earlier in the paper, we rationalized the existence of inflection points ϕ_s at r_i through the presence of a maximum ϕ_u and minima ϕ_{iH}, ϕ_{iL}. Both high and low values, ϕ_{sH} and ϕ_{sL}, satisfy $f^{(2)} = 0$ and exist at all interfaces. Figure 7(a), for example, explicitly shows the mathematical features [ϕ_{iH}, ϕ_{iL} (solid line), ϕ_{sH}, ϕ_{sL} (dash-dotted line), ϕ_u (dashed line), and critical point] occurring at r_i with changing T in an open
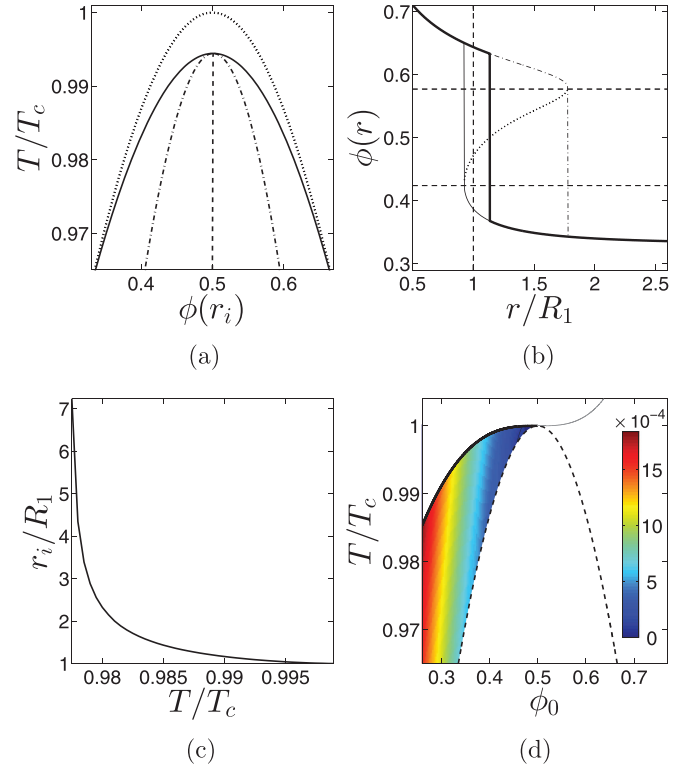

FIG. 7. (Color online) Electrostatic spinodal for an open cylinder system. (a) Behavior of $\phi(r_i)$ with T, showing ϕ_{iH}, ϕ_{iL} (solid line), ϕ_{sH}, ϕ_{sL} (dash-dotted line), and ϕ_u (dashed line). Lines converge at the critical point ϕ_{iC}. For all data, $\phi_0 = 0.33$ and $\sigma \approx 2.09 \times 10^{-3}$ C/m^2. Dotted lines show ϕ_b. (b) All $\phi(r)$ solutions to $f' = 0$ versus normalized r. Thin solid, dash-dotted, and dotted lines show lower, upper, and unstable solutions, respectively, for $\phi_0 = 0.33$, $T/T_c = 0.975$, and $\sigma = 8 \times 10^{-4}$ C/m^2. The thick line shows the solution that minimizes f. Horizontal dashed lines show ϕ_{sL} and ϕ_{sH}. (c) Location of the interface r_i versus normalized T along the spinodal line in Fig. 6(a) for $\sigma = 1 \times 10^{-3}$ C/m^2. (d) Overlay of electrostatic spinodals for many σ [color (C/m^2)].

cylinder system. For comparison, the dotted lines display the behavior of the binodal points ϕ_b with T.

Despite the ubiquitous presence of ϕ_{sH} and ϕ_{sL}, only ϕ_{sL} carries physical meaning in open systems, and only in a limited region of the stability diagram. To see how this occurs, we return to the solutions of $f' = 0$. Thus far, we have focused on r_i, the location of the interface for the minimized f; however, there can be many r that possess the same mathematical features. Figure 7(b) shows all possible solutions to $f' = 0$, where the thin solid, dash-dotted, and dotted lines are the "lower," "upper," and "unstable" solutions, respectively. The thick solid line depicts the solution that actually minimizes f, and the two dashed lines denote ϕ_{sH} and ϕ_{sL} found at r_i.

We start from a homogeneous mixture at composition ϕ_0 and perform the thought experiment of turning on an electric field. Considering diffusive liquid movement in the absence of other factors (e.g., liquid convection and noise), this experimental setup implies that the profile $\phi(r)$ initially develops along the free energy "well" created by the lower solution. If the electric field can sufficiently "pull" the higher dielectric material such that there is at least one distance r

where $\phi(r) \geqslant \phi_{sL}$, then the liquid can escape the metastable (mixed) state at the local free energy minimum to find the global minimum (demixed). We call r_s the distance where $\phi(r_s) = \phi_{sL}$ and find r_s by solving $f' = 0$ at ϕ_{sL}. For a cylindrical geometry we have

$$\frac{r_s}{R_1} = \sqrt{\frac{Nv}{2kT\varepsilon_0}\left[\frac{\sigma^2}{f'_m(\phi_{sL}) - \mu}\right]\frac{\varepsilon'(\phi_{sL})}{\varepsilon(\phi_{sL})^2}}. \quad (17)$$

Knowing that the highest value of $\phi(r)$ occurs closest to the electrode at R_1, we seek the conditions where $r_s = R_1$. These conditions, therefore, mark the electrostatic spinodal: If $r_s \geqslant R_1$ at a particular (ϕ_0, T, σ), then demixing occurs spontaneously. If $r_s < R_1$ at a particular (ϕ_0, T, σ) [for example Fig. 7(b)], then the liquids can be metastably mixed. The long-time solution for dynamics in these cases therefore resides along the thin solid curve [Fig. 7(b)].

Figure 6(a) shows the location of the electrostatic spinodal for a particular value of σ. The curve begins at the critical point (ϕ_K, T_K) and travels down, on the right side of the stability diagram boundary. Similarly to the regular spinodal curve, demixing occurs spontaneously (nonspontaneously) for (ϕ_0, T) to the right (left) of the electrostatic spinodal. Since the electrostatic spinodal cuts inside the stability diagram, the location of the interface r_i emerges at distances greater than R_1, with $r_i = R_1$ only at (ϕ_K, T_K). Figure 7(c) displays the behavior of r_i along the spinodal in Fig. 6(a). Finally, the electrostatic spinodal exists for all σ. Figure 7(d) shows the superposition of the electrostatic spinodal curves, where the color indicates the associated σ.

VIII. CLOSED SYSTEMS

So far, we have focused on liquid behavior in open systems, where we consider the location of the second boundary as $R_2 \to \infty$. A closed system with a finite R_2 markedly alters the phase diagram [16]; however, we show that these alterations naturally arise from the solutions of open systems.

We begin as previously, with variations in the concentration profiles $\phi(r)$, and identify interesting changes with two parameters, σ and R_2. Both Figs. 8(a) and 8(b) clearly reveal that the discontinuity at the interface decreases and vanishes with increasing σ and decreasing R_2, respectively, in closed cylinder systems. Intriguingly, the profiles in Fig. 8(a) stand in sharp contrast to the self-similar solutions found in open systems [Figs. 4(a) and 4(b)]. Closer inspection of Fig. 8(a) also reveals that the parabolic-like shape in the discontinuity with various σ opens to the left, rather than to the right as in Figs. 4(c), 4(d), and 8(b). An important consequence is that for closed systems there are *two* transition surface charge densities σ_t: the first σ_{t1} is the σ that places r_i exactly at R_1, while the second σ_{t2} is the σ where the interface discontinuity vanishes. Therefore, the interface between the liquids in closed systems only exists when σ satisfies $\sigma_{t1} \leqslant \sigma \leqslant \sigma_{t2}$ [shaded region in Fig. 8(c)].

Material conservation drives all differences between closed and open systems, thus, the key to understanding these differences resides in understanding μ. Recall that $\mu = \mu_0 = f'_m(\phi_0, T)$ in open systems, while μ is adjusted to account for material conservation in closed systems. Mathematically, the
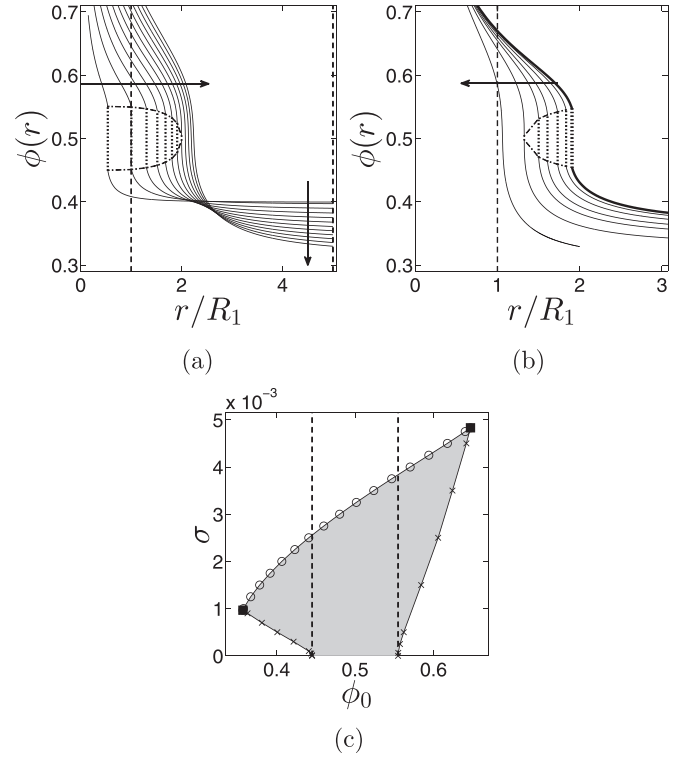

FIG. 8. Variation of concentration profiles $\phi(r)$ in a closed cylinder system. (a) $\phi(r)$ versus a normalized distance r for a constant $\phi_0 = 0.4$, $T/T_c \approx 0.996$, $R_2/R_1 = 5$ and varying $\sigma = 0.25 \times 10^{-3}$ to 3×10^{-3} C/m^2 in 0.25×10^{-3} increments (arrows). (b) $\phi(r)$ versus a normalized distance r for a constant $\phi_0 = 0.36$, $T/T_c \approx 0.995$, $\sigma = 1.5 \times 10^{-3}$ C/m^2 for an open system (thick line) and closed systems (thin lines) with decreasing $R_2/R_1 = 20$, 12, 8, 6, 4, 2 (arrow). (c) σ_{t1} ($\times$), σ_{t2} ($\circ$), and σ_K (filled squares) versus ϕ_0 for $T/T_c = 0.996$ and $R_2/R_1 = 5$. Dashed lines show the binodal ϕ_b at same T. Phase separation occurs in the shaded region.

adjusted μ for a closed system at (ϕ_0, T) exactly matches the μ_0 for an open system with a different "effective" concentration ϕ_E in the bath. Consequently, the $\phi(r)$ profile between R_1 and R_2 at (ϕ_0, T) in a closed system exactly matches the $\phi(r)$ profile at (ϕ_E, T) in an open system. In other words, the behavior of a closed system maps onto that of an open system via ϕ_E.

We can explain the variation of $\phi(r)$ with σ in closed systems using this construct. Intuitively, the higher dielectric material is pulled closer to the electrode as the value of σ increases. In order to conserve material in a closed system, $\phi(r)$ necessarily decreases near R_2 [Fig. 8(a)]. This shift in liquid concentration translates as a decrease in ϕ_E, hence an increasing σ in a closed system maps as an increasing σ *and* a decreasing ϕ_E in an open system. Recall that the interface discontinuity becomes smaller with lower ϕ_E in an open cylinder system [Fig 4(c)] and eventually vanishes when ϕ_E crosses the electrostatic binodal. The same principles apply to closed systems, where the second transition σ_{t2} marks this crossing.

Now that we understand how experimental parameters change $\phi(r)$, we focus on how these changes affect the stability diagram. Figure 9(a) shows a typical stability diagram for a constant $\sigma = 1 \times 10^{-3}$ C/m^2 and $R_2/R_1 = 5$ in a closed cylinder system. One striking difference between open
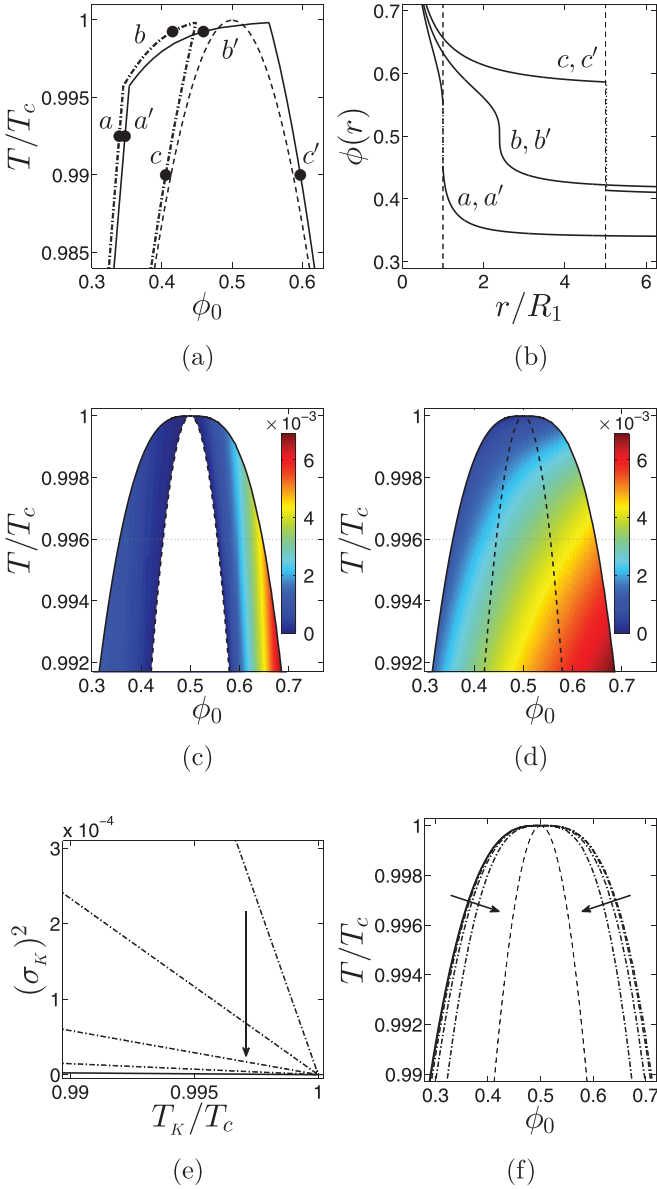
FIG. 9. (Color online) Electrostatic binodal in a closed cylinder system. (a) Stability curve (solid line) in ϕ_0-T space for a constant $\sigma = 1 \times 10^{-3}$ C/m^2 and $R_2/R_1 = 5$. The dash-dotted line shows the mapping of the stability diagram boundaries to an open system via ϕ_E (see text). The dashed line shows the binodal curve. (b) $\phi(r)$ versus normalized r for points marked by symbols in (a). Dashed lines mark the boundaries of the container. (c), (d) Overlay of many stability diagrams, where color indicates transition σ_{t1} and σ_{t2} (C/m^2), respectively. Dotted lines show the location of data in Fig. 8(c). (e) Critical surface charge density σ_K on the electrostatic binodal for $\phi_K \leqslant \phi_c$ (solid line) and $\phi_K \geqslant \phi_c$ (dash-dotted lines) for $R_2 = 20$, 10, 5, and 2.5 μm (arrow). (f) Electrostatic binodal for open (solid line) and closed (dash-dotted lines) systems for the same R_2 as in (e). Curves are *not* symmetric around $\phi_0 = 0.5$. The dashed line shows the binodal curve.

[Fig. 6(a)] and closed [Fig. 9(a)] systems is that liquid separation can now occur for $\phi_0 > \phi_c$. Experimentally, this manifests as an interface emerging close to R_2, rather than R_1. The second, more subtle difference is that the stability diagram for closed systems occupies a slightly smaller region of ϕ_0-T

space for $\phi_0 \leqslant \phi_c$ compared to open systems with the same σ. Finally, the upper boundary for the closed-system stability curve travels *below T_c* to *exclude* a portion of the binodal curve. Closed systems, therefore, provide the interesting possibility of an electric field mixing liquids that normally demix.

We can use the mapping construct not only to comprehend these changes but also to produce the stability diagram of a closed system. Open systems link to closed systems via integration. Specifically, integrating $\phi(r)$ between R_1 and R_2 in an open system at (ϕ_E, T) gives the corresponding (ϕ_0, T) for the closed system. We begin with the left boundary of the stability diagram for an open system [a in Fig. 9(a)] and integrate $\phi(r)$ between R_1 and R_2 to determine the location of the left boundary in a closed system [a' in Fig. 9(a)]. The difference between ϕ_E and ϕ_0 along this boundary is small. If we look at an example $\phi(r)$ profile [Fig. 9(b)], we see that the interface location r_i equals R_1 and that the electric field for $r > R_1$ produces only small variations in $\phi(r)$. Truncating the integration at R_2, therefore, only minimally alters the liquid concentration.

Next, we consider the upper boundary of the open-system stability diagram [b in Fig. 9(a)], and integrate from R_1 to R_2 to obtain the upper boundary for the closed-system stability diagram [b' in Fig. 9(a)]. Here, large differences between ϕ_E and ϕ_0 can occur. This boundary for open systems is the electrostatic binodal. As described in Sec. VI, $\sigma > \sigma_K$, which causes the location of the interface r_i to emerge at distances greater than R_1. The inclusion of high-dielectric material from R_1 to r_i can substantially increase ϕ_0 when integration stops at R_2.

The upper boundary of the stability diagram for a closed system ends when $r_i = R_2$. And to form the right boundary in a closed system, we must find the conditions where σ places r_i at R_2 in an open system. There are two methods by which to proceed. First, we present the simple straightforward approach. We use Eq. (10) with σ, $r_i = R_2$, and various T to determine the appropriate ϕ_E [c in Fig. 9(a)] and then integrate $\phi(r)$ profiles from R_1 to R_2 to create the right boundary for the closed system [c' in Fig. 9(a)]. The second method relies on the self-similarity of the solutions in open systems. We recognize that line c in Fig. 9(a) is the stability line (where $r_i = R_1$) for a rescaled surface charge, namely, $\sigma R_1/R_2$ for cylindrical geometry. The ability to shift the interface and rescale the solution with a modified σ will prove useful in creating the closed-system electrostatic binodal.

The superposition of the stability diagrams from many σ produces Figs. 9(c) and 9(d), where color indicates σ_{t1} and σ_{t2}, respectively, for $R_2/R_1 = 5$. These figures reveal striking asymmetry with respect to ϕ_c in the values of both σ_{t1} and σ_{t2}. Notably, higher σ are necessary both to create (σ_{t1}) and eventually to destroy (σ_{t2}) the interface when $\phi_0 > \phi_c$. The outer bounding line in Figs. 9(c) and 9(d) represents the electrostatic binodal for a closed system. This line is also asymmetric with respect to ϕ_c. And due to the structure of the stability diagram in closed systems, σ_K is both σ_{t1} *and* σ_{t2} for all (ϕ_K, T_K) [see Fig. 8(c)].

In order to find this electrostatic binodal, we follow the same methods we used to find the stability diagram of the closed system. We begin with the open-system solutions at $(\phi_E = \phi_K, T = T_K, \sigma = \sigma_K)$ and integrate $\phi(r)$ between R_1
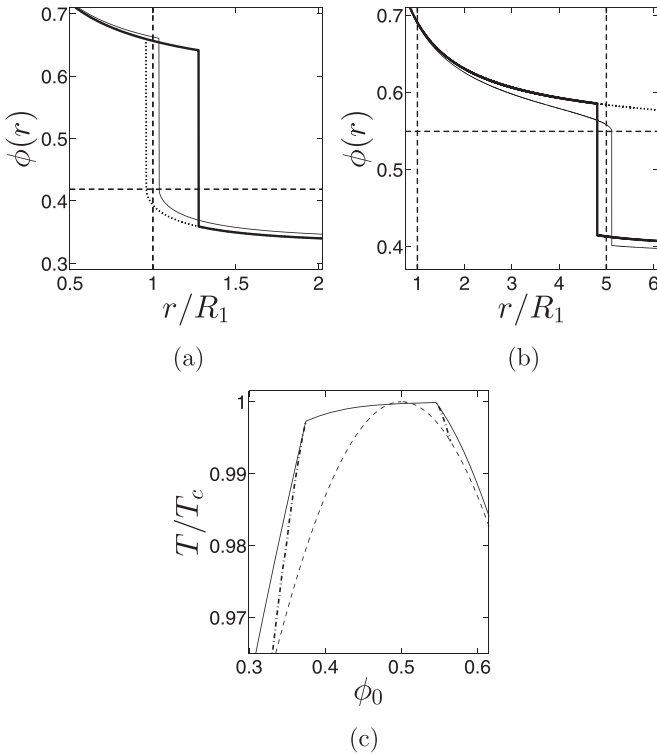
FIG. 10. Electrostatic spinodal in closed systems. (a) $\phi(r)$ versus normalized r for $\phi_0 \approx 0.34$, $T/T_c \approx 0.973$, $\sigma = 8 \times 10^{-4}\,\mathrm{C/m^2}$, and $R_2/R_1 = 5$ for the minimized solution to f (thick solid line) and lower metastable solution (thin solid line). The horizontal dashed line shows ϕ_{sL}. The thick solid line also shows the minimized open-system solution for $\phi_E = 0.33$, while the dotted line shows the corresponding lower solution. (b) $\phi(r)$ versus normalized r for $\phi_0 \approx 0.59$, $T/T_c = 0.99$, $\sigma = 1.46 \times 10^{-3}\,\mathrm{C/m^2}$, and $R_2/R_1 = 5$ for the minimized solution to f (thick solid line) and upper metastable solution (thin solid line). The horizontal dashed line shows ϕ_{sH}. The thick solid line also shows the minimized open-system solution for $\phi_E \approx 0.40$, while the dotted line shows the corresponding upper solution. (c) Stability diagram (solid curve) with spinodal lines (dash-dotted curves) for $\sigma = 8 \times 10^{-4}\,\mathrm{C/m^2}$ and $R_2/R_1 = 5$. The dashed line is the binodal curve.

and R_2 to determine ϕ_0 (the ϕ_K for the closed system). Note that this procedure accounts for interfaces emerging at R_1; however, closed systems can also have interfaces emerging from R_2. Therefore, we rescale the open-system solutions by increasing σ so that $r_i = R_2$ [precisely ($\phi_E = \phi_K$, $T = T_K$, $\sigma = \sigma_K R_2/R_1$) for cylindrical geometry] and integrate $\phi(r)$. This rescaling links σ and R_2, as is evident in Fig. 9(e). Consequently, phase separation for concentrations higher than ϕ_c technically exists for open systems and requires infinitely large σ to produce an interface at $R_2 \to \infty$. Practically speaking, however, even closed systems with a "large enough" R_2 would need unreasonably high values of σ to induce a transition in this region of ϕ_0-T space. Under these conditions, other events, such as heating, liquid ionization, bubble formation, and electrical breakdown of the liquids, would need to be considered [25–27].

Figure 9(f) shows how the electrostatic binodal changes with R_2, where the curve surrounds a smaller region of ϕ_0-T

space as R_2 decreases. This change, however, is relatively minor, unless R_2/R_1 becomes sufficiently "small."

Material conservation produces two spinodal lines in a closed system—one line associated with each boundary. Finding the spinodal line associated with R_1 consists of finding $\phi(r_s) = \phi_{sL}$ on the lower solution of f and ensuring $r_s = R_1$, similarly to open systems. However, the lower solution from ϕ_E in an open system does not fulfill the material conservation requirement. Instead, the lower solution from yet another open-system concentration ϕ_E must be used. Figure 10(a) shows example $\phi(r)$ profiles associated with R_1. The thick line corresponds to the profile $\phi(r)$ that satisfies the free energy minimum of f, the dotted line is the lower solution for the open system, and the thin line is the lower solution for the closed system with $R_2/R_1 = 5$. In Fig. 10(a), the open system could be in a metastable state (compare thick solid and dotted lines), while the closed system would not be metastable (compare thick and thin solid lines). Similar behavior applies for the location of the spinodal line at R_2; however, this line consists of finding $\phi(r_s) = \phi_{sH}$ on the *upper* solution of f. The line styles in Fig. 10(b) are as those in Fig. 10(a). In Fig. 10(b), the closed system could be metastable, while the open system would not be metastable (recall that the upper solutions have no meaning in open systems).

Finally, Fig 10(c) shows the location of the electrostatic spinodal lines in a closed system for particular values of σ and R_2/R_1. Each line begins at the critical points (ϕ_K, T_K) on either side of ϕ_c and travels down "inside" the stability diagram.

IX. CONCLUSION

In summary, we have described the mixing-demixing phase diagram for two dielectric liquids in an electric field. By focusing on the liquid-liquid interface and adapting standard methods for determining phase diagrams, we have found the electrostatic equivalent of binodal lines, spinodal lines, and critical points. Given this new perspective, the dynamics of phase separation with nonuniform electric fields requires reinvestigation, with an emphasis on validating predicted metastable states and uncovering critical dynamic behavior. Perhaps similar adaptations of existing theory for dynamics will uncover new features in the electric-field modified liquid-liquid phase diagram.

In addition, we have restricted our analysis to solutions with radial symmetry, enforcing one-dimensional solutions that depend only on the distance r. This constraint, however, might not satisfactorily apply to all experimental conditions, and allowing for full two- or three-dimensional theoretical investigations could uncover non–radially symmetric solutions. For example, interfacial energies, both liquid-liquid and liquid-surface energies, dominate the liquid patterning for phase separation beneath the regular binodal curve in the absence of a field. And in the case where both liquids have an equal preference for the surface, liquid-liquid interfaces emerge normal to a surface. This configuration, however, can be electrostatically unfavorable since the low-dielectric material is adjacent to the charge. It will be interesting to determine if, when, and how instabilities in the interface develop and whether these instabilities modify the phase diagram.

Also, highly confined cylindrical geometries do not show a true liquid-liquid phase transition [28]. Here, the system can be approximated as one-dimensional, with the expectation that correlations diverge as the length of the cylinder goes to infinity. It is unknown whether the addition of a nonuniform electric field is sufficient to induce a true transition in this case. An appropriate investigation on this topic would, of course, require theories that go beyond the mean-field approach.

Finally, we have not considered the fluid wetting behavior on the electrode surfaces. In the wedge geometry, for example, these phenomena include wedge filling, where a liquid transitions between partial and complete filling [29–31]. This transition can be either first or second order and depends on factors like the wedge opening angle, liquid contact angle, and temperature. Since our results show that the interface location directly ties with the electric field, it currently remains unclear whether the electric field enhances or diminishes the effects of wetting, or possibly both (depending on the experimental conditions).

[1] M. R. Moldover, J. V. Sengers, R. W. Gammon, and R. J. Hocken, Rev. Mod. Phys. **51**, 79 (1979).

[2] A. Asamitsu, Y. Moritomo, Y. Tomioka, T. Arima, and Y. Tokura, Nature **373**, 407 (1995).

[3] L. D. Landau and E. M. Lifshitz, *Elektrodinamika Sploshnykh Sred* (Nauka, Moscow, 1957), Chap. 2, Sec. 18, Problem 1.

[4] A. Silberberg and W. Kuhn, Nature **170**, 450 (1952).

[5] A. I. Nakatani, F. A. Morrison, J. F. Douglas, J. W. Mays, C. L. Jackson, M. Muthukumar, and C. C. Han, J. Chem. Phys. **104**, 1589 (1996).

[6] A. Onuki, Europhys. Lett. **29**, 611 (1995).

[7] A. Onuki, Physica A **217**, 38 (1995).

[8] S. Stepanow and T. Thurn-Albrecht, Phys. Rev. E **79**, 041104 (2009).

[9] P. Debye and K. Kleboth, J. Chem. Phys. **42**, 3155 (1965).

[10] D. Beaglehole, J. Chem. Phys. **74**, 5251 (1981).

[11] M. D. Early, J. Chem. Phys. **96**, 641 (1992).

[12] D. Wirtz and G. G. Fuller, Phys. Rev. Lett. **71**, 2236 (1993).

[13] K. Orzechowski, Chem. Phys. **240**, 275 (1999).

[14] Y. Tsori, F. Tournilhac, and L. Leibler, Nature **430**, 544 (2004).

[15] G. Marcus, S. Samin, and Y. Tsori, J. Chem. Phys. **129**, 061101 (2008).

[16] S. Samin and Y. Tsori, J. Chem. Phys. **131**, 194102 (2009).

[17] A. Aharony, Phys. Rev. B **18**, 3318 (1978).

[18] R. L. C. Vink and A. J. Archer, Phys. Rev. E **85**, 031505 (2012).

[19] S. Safran, *Statistical Thermodynamics of Surfaces, Interfaces, and Membranes* (Westview Press, New York, 1994).

[20] J. V. Sengers, D. Bedeaux, P. Mazur, and S. C. Greer, Physica **104**, 573 (1980).

[21] J. Leys, P. Losada-Pérez, G. Cordoyiannis, C. A. Cerdeiriña, C. Glorieux, and J. Thoen, J. Chem. Phys. **132**, 104508 (2010).

[22] M. F. Hsu, E. R. Dufresne, and D. A. Weitz, Langmuir **21**, 4881 (2005).

[23] S. Samin and Y. Tsori, J. Phys. Chem. B **115**, 75 (2011).

[24] K. Binder, in *Kinetics of Phase Transitions*, edited by S. Puri and V. Wadhawan (CRC Press, Boca Raton, FL, 2009), p. 6399.

[25] R. Coelho and J. Debeau, J. Phys. D: Appl. Phys. **4**, 1266 (1971).

[26] W. F. Schmidt, IEEE T. Electr. Insul. **19**, 389 (1984).

[27] A. Denat, J. P. Gosse, and B. Gosse, IEEE T. Electr. Insul. **23**, 545 (1988).

[28] A. Winkler, D. Wilms, P. Virnau, and K. Binder, J. Chem. Phys. **133**, 164702 (2010).

[29] A. O. Parry, C. Rascón, and A. J. Wood, Phys. Rev. Lett. **83**, 5535 (1999).

[30] A. O. Parry, C. Rascón, and A. J. Wood, Phys. Rev. Lett. **85**, 345 (2000).

[31] L. Bruschi, A. Carlin, and G. Mistura, Phys. Rev. Lett. **89**, 166101 (2002).